



Article

Highly Active Amino-Fullerene Derivative-Modified TiO₂ for Enhancing Formaldehyde Degradation Efficiency under Solar-Light Irradiation

Jingbiao Fan ¹, Tao Wang ^{1,2}, Bo Wu ^{1,2,*} and Chunru Wang ^{1,2,*}

¹ Beijing National Laboratory for Molecular Sciences, Key Laboratory of Molecular Nanostructure and Nanotechnology, Institute of Chemistry, Chinese Academy of Sciences, Beijing 100190, China; fanjingbiao6277@163.com (J.F.); wangtaojk2007@163.com (T.W.)

² University of Chinese Academy of Sciences, Beijing 100049, China

* Correspondence: zkywubo@iccas.ac.cn (B.W.); crwang@iccas.ac.cn (C.W.)

Abstract: Formaldehyde (HCHO) is a ubiquitous indoor pollutant that seriously endangers human health. The removal of formaldehyde effectively at room temperature has always been a challenging problem. Here, a kind of amino-fullerene derivative (C₆₀-EDA)-modified titanium dioxide (C₆₀-EDA/TiO₂) was prepared by one-step hydrothermal method, which could degrade the formaldehyde under solar light irradiation at room temperature with high efficiency and stability. Importantly, the introduction of C₆₀-EDA not only increases the adsorption of the free formaldehyde molecules but also improves the utilization of sunlight and suppresses photoelectron-hole recombination. The experimental results indicated that the C₆₀-EDA/TiO₂ nanoparticles exhibit much higher formaldehyde removal efficiency than carboxyl-fullerene-modified TiO₂, pristine TiO₂ nanoparticles, and almost all other reported formaldehyde catalysts especially in the aspect of the quality of formaldehyde that is treated by catalyst with unit mass ($m_{\text{HCHO}}/m_{\text{catalyst}} = 40.85 \text{ mg/g}$), and the removal efficiency has kept more than 96% after 12 cycles. Finally, a potential formaldehyde degradation pathway was deduced based on the situ diffuse reflectance infrared Fourier transform spectrometry (DRIFTS) and reaction intermediates. This work provides some indications into the design and fabrication of the catalysts with excellent catalytic performances for HCHO removal at room temperature.

Keywords: amino-fullerene derivative; photocatalysis; chemical adsorption; HCHO degradation; TiO₂ nanoparticle



Citation: Fan, J.; Wang, T.; Wu, B.; Wang, C. Highly Active Amino-Fullerene Derivative-Modified TiO₂ for Enhancing Formaldehyde Degradation Efficiency under Solar-Light Irradiation. *Nanomaterials* **2022**, *12*, 2366. <https://doi.org/10.3390/nano12142366>

Academic Editor: Antonino Gulino

Received: 28 June 2022

Accepted: 8 July 2022

Published: 11 July 2022

Publisher's Note: MDPI stays neutral with regard to jurisdictional claims in published maps and institutional affiliations.



Copyright: © 2022 by the authors. Licensee MDPI, Basel, Switzerland. This article is an open access article distributed under the terms and conditions of the Creative Commons Attribution (CC BY) license (<https://creativecommons.org/licenses/by/4.0/>).

1. Introduction

Formaldehyde (HCHO) is a main pollutant in indoor environments, which can be absorbed by the human body through different channels and may be a serious harm to people's health. The toxicity of formaldehyde is well-known and it is classified as a human carcinogen, which have made it an important risk to human health, even at low concentrations. It causes respiratory problems, leukemia, asthma, and other diseases [1–4]. Therefore, the effective removal of formaldehyde in the environment is a necessity [5–9]. Photocatalysis is an appropriate and promising technology for environmental applications, of which the absorption of photon energy from solar-light by photocatalysts can drive redox reactions of formaldehyde at room temperature [10–13]. Titanium dioxide (TiO₂) is a kind of widely used photocatalytic material due to its excellent properties of low price, high activity, chemical stability, and nontoxicity [14–17]. However, as restricted by the wide bandgap (up to 3.2 eV) and the fast electrons and holes recombination rate [18,19].

The suitable particle size, optimized coating, and doping pure TiO₂ with ions have always been the methods to increase the photocatalytic activity. Among the TiO₂-supporting noble metals, Pt [20] and Au [21] have been regarded as the most active for formaldehyde degradation. However, the high price of noble metals greatly limits its large-scale

application [22]. The unique physical and chemical properties of fullerenes have led many researchers to investigate the application of this molecule and its functionalized derivatives in various fields such as medicine, photovoltaics, gas adsorption/storage, and pharmaceuticals [12]. Many fullerene-semiconductor materials have been successfully developed for photocatalytic applications, such as $\text{TiO}_2/\text{C}_{60}$ [23], $\text{TiO}_2/\text{C}_{70}$ [24], ZnO/C_{60} [25], CdS/C_{60} [13,26], and $\text{C}_3\text{N}_4/\text{C}_{60}$ [27,28]. These photocatalysts have been extensively studied for photocatalytic degradation of pollutants [29], disinfection [30], and water splitting for H_2 evolution [13]. Typically, the C_{60} - TiO_2 nanocomposites have been reported to be able to efficiently catalyze degradation multiple organic substrates [12]. The incorporated C_{60} not only inhibits the charge recombination, but also broadens the light absorption range to a certain degree [23,26,30–33]. Nevertheless, the photocatalytic performance and the range of application of this kind of composites is still not satisfactory.

In pursuit of the high photocatalytic efficiency, the chemical adsorption plays an important role in formaldehyde removal. It has been reported that S- and N-containing functional groups (pyridines, amines, and sulfones/sulfonic acids) considerably enhanced the formaldehyde adsorption ability of carbonaceous adsorbents at ambient conditions [34,35]. Ma et al. [36] have synthesized an amino-functionalized graphene aerogel. As the carbonyl, carboxyl, and epoxy groups on the graphene layers were connected to the amino groups ($-\text{NH}_2$), the molecular structure of HCHO was destroyed after being captured by the 3D structure of the aerogels. Significantly, the reaction of formaldehyde and $-\text{NH}_2$ on the graphene sheets has dramatically promoted the catalytic activities.

Bearing the aforementioned in mind, herein, we have utilized amino-fullerene derivatives (C_{60} -EDA) and TiO_2 and constructed a novel nanocomposite for the first time. The introduction of the amino group has played a crucial role in improving the adsorption performance of materials through its specific binding with formaldehyde molecules [34,36–39], which was investigated by using in situ diffuse reflectance infrared Fourier transform spectrometry (DRIFTS). The obtained C_{60} -EDA/ TiO_2 nanoparticles with a high utilization rate of sunlight and reinforced charge separation interaction, lead to enhanced photocatalytic degradation efficiency of formaldehyde.

2. Materials and Methods

2.1. Preparation of Photocatalysts

Tetrabutyl titanate (90 mL) was slowly poured into the aqueous solution. After continued stirring for 30 min, the mixed system was transferred to a 1 L reactor for hydrothermal reaction at $160\text{ }^\circ\text{C}$ for 6 h. After the reaction was completed, the supernatant was removed and the crude products were centrifugally washed with deionized water and anhydrous ethanol for several times. Finally, the obtained products were air-dried at $60\text{ }^\circ\text{C}$ for 12 h to obtain the pure TiO_2 nanoparticles.

The synthesis of amino-fullerene derivatives (C_{60} -EDA) and carboxyl-fullerene derivatives (C_{60} -COOH) were followed the same procedures that were described in Ref. [40] and Ref. [41], respectively. Then, 212 mg C_{60} -EDA or C_{60} -COOH (mass ratio is 1 wt%) was dissolved into 450 mL deionized water to prepare an aqueous solution of fullerene derivatives, and 90 mL tetrabutyl titanate was slowly poured into the aqueous solution. After continued stirring for 30 min, the mixed system was transferred to a 1 L reactor for hydrothermal reaction at $160\text{ }^\circ\text{C}$ for 6 h. After the reaction was completed, the supernatant was removed and the crude products were centrifugally washed with deionized water and anhydrous ethanol for several times. Finally, the obtained products were air-dried at $60\text{ }^\circ\text{C}$ for 12 h to obtain the C_{60} -EDA/ TiO_2 or C_{60} -COOH/ TiO_2 composite.

2.2. Characterization of Photocatalysts

The morphology and structure of the samples were determined by scanning electron microscopy (JSM-6700F JEOL), energy dispersions spectroscopy (EDS), transmission electron microscopy (TEM), and high resolution TEM (HRTEM, JEM-2100F, JEOL). The phase structure of the composites was analyzed by X-ray diffractometer under 35 kV Cu

K α radiation source. Raman spectra were performed at room temperature with a 532 nm laser as the excitation source using Thermo Scientific spectrometer. BaSO₄ was used as the reflectance standard material, and the UV-visible diffuse reflectance spectrum (DRS) of the material was measured by UV-visible diffuse reflectance spectrophotometer (UV-3100, Shimadzu Inc., Kyoto, Japan). The chemical states of the elements in the samples were analyzed by X-ray photoelectron spectroscopy (XPS, XSAM800, Kratos Analysis, Manchester, UK). Electron paramagnetic resonance (EPR) measurements were performed on a JEOL JE-FA200 spectrometer. Photochemical measurements were performed at an electrical workstation (CHI660E) using a conventional three-electrode system. Platinum wire and saturated calomel electrode (SCE) were used as counter electrode and reference electrode, respectively. The photocatalyst (5 mg) was dispersed in ethanol (0.5 mL) to obtain the grout, and then 20 μ L of the grout was coated on ITO glass and dried overnight to obtain the working electrode. A 300 W xenon lamp with an AM 1.5 filter was used as the light source and 0.5 mol L⁻¹ Na₂SO₄ solution as the electrolyte. The photocurrent response was recorded at a constant potential of 0.2 V. Electrochemical impedance spectroscopy (EIS) was performed at open circuit voltage, frequency of 0.05–10⁵ Hz, and amplitude of 5 mV. A Thermo Nicolet 6700 Fourier transform infrared (FTIR) spectrometer that was equipped with a mercury cadmium telluride (MCT) detector was used for the diffuse reflectance FTIR spectra measurements (DRIFTS). A praying mantis diffuse reflectance accessory and a reaction cell that was equipped with a heater (Harrick Scientific) were employed for the in situ sample treatment, photocatalytic reaction, and IR detection, as described in Refs. [42,43]. The TiO₂ or C₆₀-EDA/TiO₂ powder samples, which were pressed into 7 mm \times 1.5 mm cylindrical pellets (50 mg), were housed in a sample cup inside the reaction cell (Figure S1). Before the IR measurement, the samples that were filled in the sample cup were pretreated for 10 min under Ar flow (40 mL min⁻¹, open switch valve I) to remove the adsorbed impurities, and the spectra of KBr were recorded for background removal. Subsequently, the O₂ flow (10 mL min⁻¹, open switch valve II) was bubbled through saturator containing formaldehyde, and then supplied to the reaction cell under dark conditions. The above process is called the HCHO adsorption process in the discussion of the paper, which was carried out for 70 min under dark, and the total gas flow rate was 50 mL/min (O₂ flow: 10 mL min⁻¹, Ar flow: 40 mL min⁻¹). Finally, the O₂ flow (10 mL min⁻¹, open switch valve III and close switch valve II) was directly supplied to the reaction cell. Meanwhile, the catalysts were illuminated by a 300 W xenon lamp with an AM 1.5 filter for 60 min. The above process is called the HCHO oxidation process in the discussion of the paper, which was carried out for 60 min under light, and the total gas flow rate was 50 mL/min (O₂ flow: 10 mL min⁻¹, Ar flow: 40 mL min⁻¹). All the spectra were recorded in the range of 650–4000 cm⁻¹ by averaging 400 scans with a resolution of 4 cm⁻¹ at scanning velocity of 20 kHz.

2.3. Photocatalytic Activity Test

The photocatalytic activity of the catalyst was tested in a homemade photoreactor (150 L, the length, width and height are 60 cm, 50 cm, and 50 cm, respectively), as shown in Figure S2. The reactor, formaldehyde detector, and gas chromatography were connected in series to form a closed-loop system. The gas in the reactor was mixed evenly and quickly through a fan. The peristaltic pump provided uniform flow power for formaldehyde in the reactor to ensure the stabilization of HCHO in the reactor and good contact between all the participants of the reaction system. Before the test, a Petri dish with a diameter of 15 cm was placed at the bottom of the reactor, containing 0.5 g sample. Then, 50 μ L HCHO solution (38%) was injected into the reactor, and the initial concentration of HCHO was adjusted to about 100 ppm by controlling the humidity in the reactor to be about 55% and the temperature to be about 28–30 °C under dark conditions. It's worth noting that the reactor needs to stand in the dark for 1 h after the injection of formaldehyde solution before proceeding to the next step to ensure that an adsorption-desorption equilibrium is established between the catalyst and formaldehyde. When the concentration of HCHO

in the reactor stabilized, the xenon lamp light source was turned on to illuminate the sample surface. The concentration of HCHO in the reactor was detected by HCHO online detector (PN-2000 sensor) in real time. Meanwhile, the CO₂ that was generated during HCHO oxidation was monitored by gas chromatography in real-time. The increase of CO₂ concentration (ppm, ΔCO₂, which is the difference between CO₂ concentrations at t reaction time and initial time) and the decrease of HCHO concentration were recorded to evaluate the adsorption and catalytic performance. The removal rate of HCHO was determined as:

$$\text{HCHO removal rate (\%)} = \frac{C_0 - C}{C_0} 100\% \quad (1)$$

where C₀ (ppm) is the initial equilibrium concentration of HCHO before the test, and C (ppm) is the final concentration of HCHO at the end of the test.

3. Results and Discussion

3.1. Morphology and Structure Characterization

The C₆₀-EDA/TiO₂ nanoparticles were synthesized using a surface-modification method. C₆₀-EDA were immobilized on the surface of TiO₂ nanoparticles in one step. The nanostructure of the sample was characterized by SEM and TEM. As shown in Figure 1a, the C₆₀-EDA/TiO₂ composite is composed of homogeneous nanoparticles with an average particle size of about 15 nm (Figure 1g). Compared with the pristine TiO₂ nanoparticles (Figure S3 in the Supplementary Materials), the morphology of C₆₀-EDA/TiO₂ composite is also the particles, and the particle size are similar, indicating that the introduction of C₆₀-EDA will not undermine the morphology of TiO₂ nanoparticles. The TEM-EDS element distribution of C₆₀-EDA/TiO₂ nanoparticles are presented in Figure 1b–f, which clearly display the C, N, O, and Ti elements are uniformly dispersed. Moreover, the XRD pattern of the initial TiO₂ nanoparticles was assigned to the typical structure of anatase phase [44] in Figure 2a. The peaks at 25.4° (101), 37.5° (004), 48.1° (200), 53.8° (105), 54.8° (211), and 62.8° (204) correspond to the pure anatase phase. After surface modification, the XRD pattern of C₆₀-EDA/TiO₂ composite display almost the same characteristic peaks as that of the pristine TiO₂. The crystalline form of TiO₂ nanoparticles remains virtually unchanged, coincident with the TEM results (Figure S4).

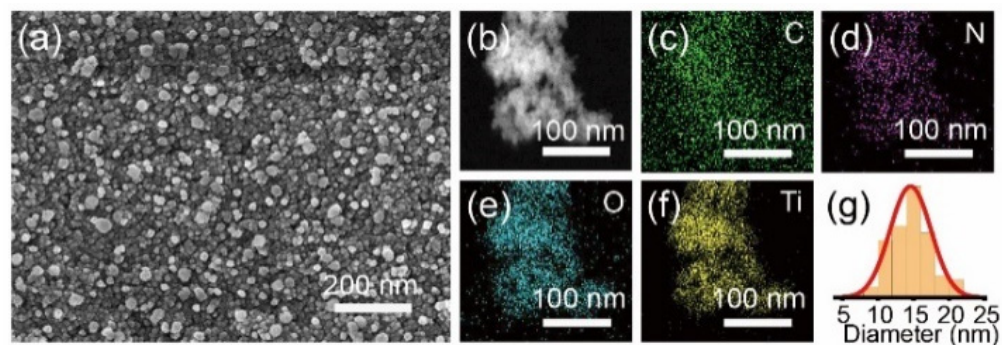


Figure 1. (a) SEM, (b) TEM, (c–f) EDS mapping, and (g) histogram of particle size distribution of C₆₀-EDA/TiO₂ composite.

To further elucidate the interaction of C₆₀-EDA and TiO₂, Raman and XPS experiments measurements were carried out. As shown in Figure 2b, the peaks of C₆₀-EDA/TiO₂ at 144, 400, 515, and 636 cm⁻¹ are the characteristic peaks of anatase TiO₂ with Eg(1), B1g(1), A1g(1), B1g(2), and Eg(2) vibration modes [17,44,45]. The fullerene-related Raman peaks appear between 1200–1600 cm⁻¹, which corresponds to the two typical peaks of C₆₀-EDA (located at 1397 and 1579 cm⁻¹), indicating the non-ignorable bond interaction between C₆₀-EDA and TiO₂ [17]. In the case of C₆₀-EDA/TiO₂ nanocomposites, N1s appeared in the XPS spectrum (Figure 2c), providing further evidence to the successfully introduce C₆₀-EDA into the composite, which was consistent with TEM-EDS mapping results. At

the same time, it can be observed that the positive displacement of Ti 2p binding energy of C₆₀-EDA/TiO₂ relative to that of TiO₂ is 0.4 eV (Figure 2d), indicating that there is an electronic interaction between C₆₀-EDA and TiO₂ [45]. It is worth noting that compared with pristine C₆₀-EDA, the binding energies of N-Hx (401.7 eV) and C-N (399.5 eV) in the N1s high-resolution spectra of C₆₀-EDA/TiO₂ (Figure S5) are positively shifted by 1.1 and 0.4 eV, respectively, which should be caused by the formation of N-O-Ti by the interaction of the amino groups on C₆₀-EDA with the hydroxyl groups on the surface of TiO₂ [16]. Electron-deficient Ti atoms tend to lower the electron density of N-O system via Ti-O bond, weakening the shielding effect of N valence electrons, thus increasing the binding energy of N1s [16,46,47].

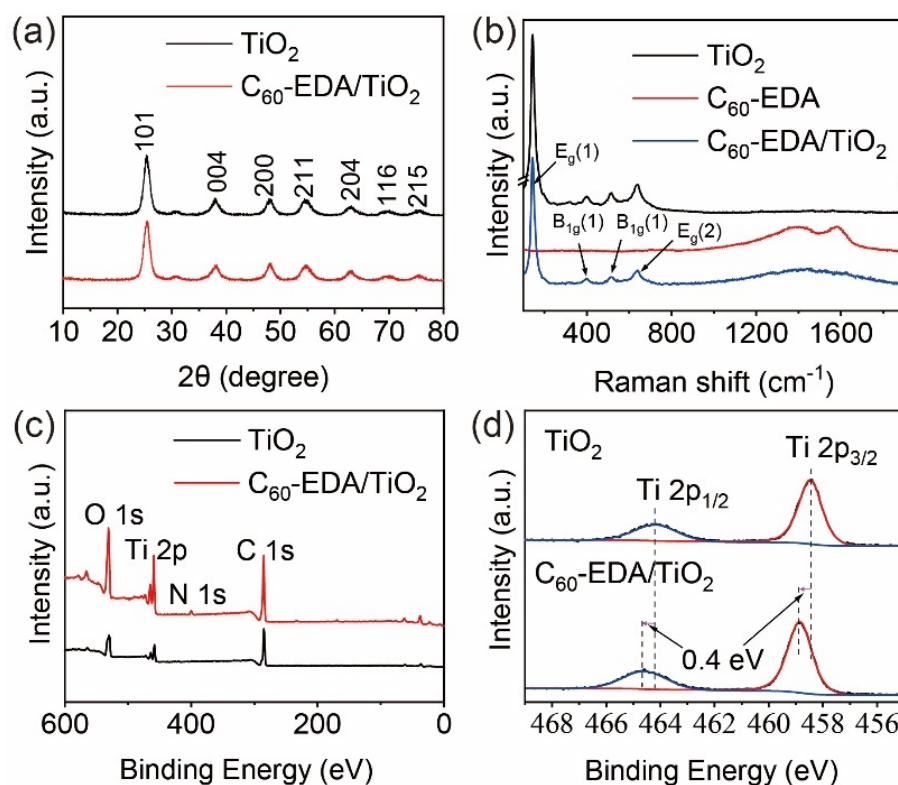


Figure 2. (a) XRD, (b) Raman, (c) full XPS, and (d) Ti 2p high-resolution spectra of pristine TiO₂ and C₆₀-EDA/TiO₂.

3.2. Photocatalytic Properties

The photocatalytic formaldehyde degradation performance of C₆₀-EDA/TiO₂ composite was tested by a self-made photocatalytic apparatus (Figure S2). As shown in Figure 3a, the formaldehyde degradation rate of C₆₀-EDA/TiO₂ sample was about 97% after 6 h with simulated sunlight irradiation, which was significantly higher than that of C₆₀-COOH/TiO₂ (89%) and pristine TiO₂ nanoparticles (32%; Figure S6). In comparison with the other reported formaldehyde catalysts [1,3,7,11,46–58] (Table S1), the catalytic activity of the C₆₀-EDA/TiO₂ composite is also significantly higher, especially in the aspect of the quality of formaldehyde that was treated by the catalyst with unit mass ($m_{\text{HCHO}}/m_{\text{catalyst}} = 40.85 \text{ mg/g}$). It is worth noting that the degradation amount of formaldehyde and the generation amount of CO₂ are close to 1:1, for example, the concentration of formaldehyde is reduced to 58 ppm after the degradation for 1 h, and the CO₂ increase from 405 ppm to 462 ppm (Figure S7). Moreover, as shown in Figure 3a, the formaldehyde degradation rate of C₆₀-EDA/TiO₂ sample was 58% after 1 h, significantly higher than that of C₆₀-COOH/TiO₂ (38%). Therefore, the amino functional groups on the surface of the catalyst play an important role in the formaldehyde degradation progress. Among, the 1 wt% C₆₀-EDA have achieved an optimal conversion efficiency (Figure S8).

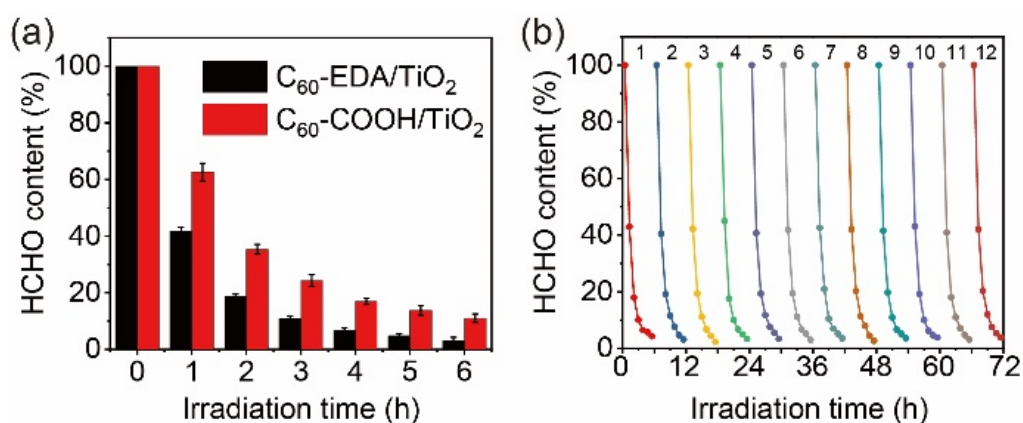


Figure 3. (a) Catalytic performance of C₆₀-EDA/TiO₂ and C₆₀-COOH/TiO₂ for the photodegradation of HCHO under simulated sunlight irradiation. (b) Cycling tests of C₆₀-EDA/TiO₂ for 12 cycles of photodegradation.

What is more, the stability of the photocatalyst is another important factor for practical use. As shown in Figure 3b, there was no obvious decrease after 12 cycle tests in the catalytic activity for C₆₀-EDA/TiO₂. The HCHO degradation rate of C₆₀-EDA/TiO₂ sample were maintained in 96% after 6 h simulated sunlight irradiation in the 12th cycles, indicating the outstanding stability of the catalyst. The SEM and XRD analysis showed that the morphology and lattice structure of the samples did not change before and after the cycle tests (Figures S9 and S10).

3.3. Mechanisms of Formaldehyde Degradation

The light absorption property of the as-prepared photocatalyst was recorded in the diffuse reflectance spectra, as shown in Figure 4a. It can be seen that pristine TiO₂ nanoparticles has almost no absorption above 400 nm, while C₆₀-EDA/TiO₂ extends the light absorption range obviously in the visible region. The band gaps of TiO₂ and C₆₀-EDA/TiO₂ are 2.96 eV and 2.5 eV, calculated by the equation $\alpha h\nu = A(h\nu - E_g)^{1/2}$, where α , ν , E_g , and A are the absorption coefficient, frequency of light, band gap, and A constant, respectively [44,59]. Compared with pristine TiO₂ nanoparticles, the C₆₀-EDA/TiO₂ composite has a higher efficiency for solar energy utilization, which makes a contribution to the improvement of the photocatalytic activity.

In order to explore the separation and recombination of photogenerated electrons and holes in the composite materials, the steady-state PL spectra of TiO₂ and C₆₀-EDA/TiO₂ in the range of 350–550 nm were recorded under UV-light irradiation of 300 nm (Figure 4b). Compared with pristine TiO₂, the PL emission intensity of the composite materials was significantly weaker. The results show that C₆₀-EDA can be used as a good acceptor of photogenerated electrons in the sTiO₂ conduction band and inhibits the recombination of photogenerated electrons and holes effectively [17,24].

To disclose the enhancing effect of C₆₀-EDA on the photocatalytic activity, the photoelectrochemical properties of the C₆₀-EDA/TiO₂ nanocomposite were systematically examined. As can be seen from Figure 4c, the C₆₀-EDA/TiO₂ composite exhibits rapid photocurrent response under simulated solar irradiation, with a response intensity up to 2.0 $\mu\text{A}/\text{cm}^2$, which is significantly higher than that of pristine TiO₂ (0.5 $\mu\text{A}/\text{cm}^2$), indicating that more photogenerated carriers can be effectively separated in the C₆₀-EDA/TiO₂ composite. It is shown that the introduction of C₆₀-EDA increases the generation and transfer of charge carriers under sunlight, and effectively inhibits the recombination of photogenerated electrons and holes [17,60]. Further, the electron transport resistance of the C₆₀-EDA/TiO₂ photocatalyst was measured by EIS in Figure 4d. Generally, each arc in the plot represents a resistance during the charge transfer process, and a smaller radius correlates to a lower charge transfer resistance [17,60]. Accordingly, the radius of

C_{60} -EDA/ TiO_2 is significantly smaller than that of pristine TiO_2 , indicating that the charge transfer resistance of the composite material is lower and the charge separation is more effective. These findings perfectly coincide with the results that were obtained from the photo-response measurements.

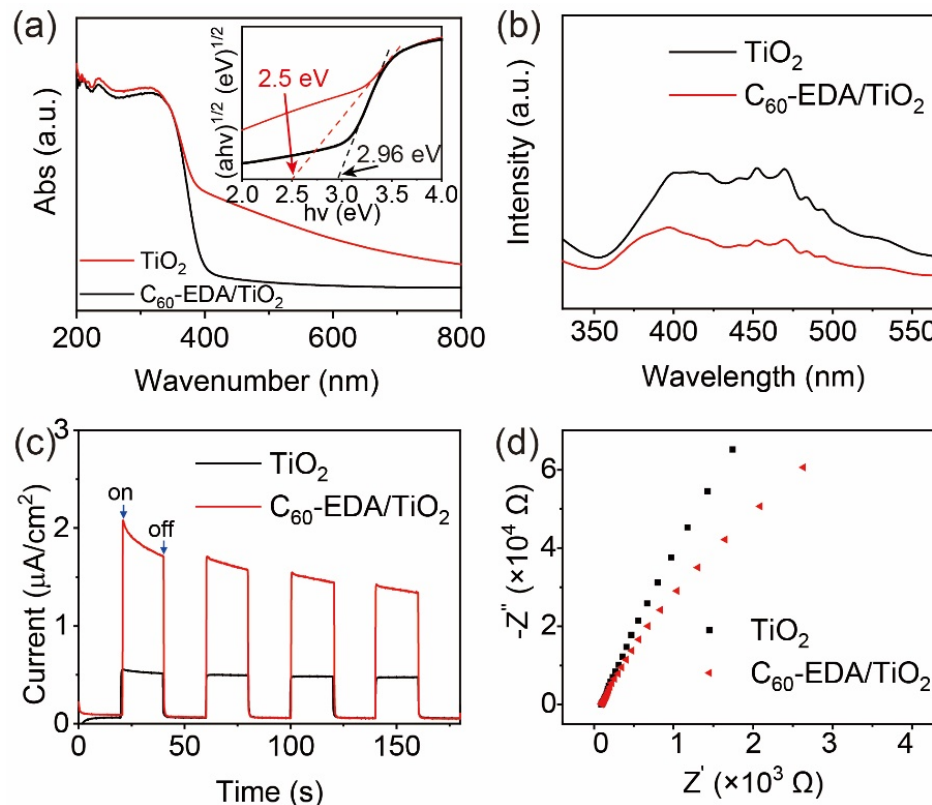


Figure 4. (a) UV diffuse reflectance spectra (inset is band gap energy diagram), (b) fluorescence spectra, (c) photocurrent response, and (d) AC impedance of TiO_2 and C_{60} -EDA/ TiO_2 .

Moreover, in order to identify the reactive radicals during the photocatalytic reaction process, in situ EPR measurements with DMPO as the spin trapping agent were performed. As displayed in Figure S11, the characteristic signals of hydroxyl radical ($\bullet OH$) and superoxide radical ($\bullet O_2^-$) were generated from the oxidation of H_2O by the photogenerated holes, and the reduction of O_2 by the photogenerated electrons [11,61–63]. The results of the EPR measurements proved that efficient separation of photogenerated electrons and holes of C_{60} -EDA/ TiO_2 has produced more reactive oxygen radicals than TiO_2 nanoparticles, so as to accelerate the reaction with formaldehyde.

To clarify, the intermediate species of the catalysts in the reaction of formaldehyde at room temperature, in situ DRIFT spectra of the TiO_2 and C_{60} -EDA/ TiO_2 materials were performed (Figure 5 and Table 1). This mainly concerned the formaldehyde adsorption and oxidation process. According to previous studies, the bands that are located around $1000\text{--}1200\text{ cm}^{-1}$ $\nu(CO)$ and 1415 cm^{-1} $\delta(CH_2)$ can be attributed to dioxymethyl (DOM) [6,7] and unstable hemiaminal [37,64]. The bands at 1578 cm^{-1} ($\nu_{as}(COO)$) and 1359 cm^{-1} ($\nu_s(COO)$) are attributed to formate and carbonate species, respectively [6]. In terms of pristine TiO_2 (Figure S12), two negative bands at 3656 cm^{-1} $\nu(OH)$ and 1716 cm^{-1} $\delta(H-O-H)$ can be ascribed to the hydroxyl $\nu(OH)$ and adsorbed water on the surface of TiO_2 nanoparticle, respectively [6,43]. It is worth noting that the bands of C_{60} -EDA/ TiO_2 at 1573 cm^{-1} $\nu(C=N)$ and $1360\text{--}1251\text{ cm}^{-1}$ $\nu(C-N)$ can be attributed to imines ($C=N$) and hemiaminal ($-NH-CH_2-OH$) [34,36,37], indicating that the chemical absorption process of HCHO was realized based on the nucleophilic addition reaction between amine ($-NH_2$) and aldehyde ($-CHO$) on the surface of the C_{60} -EDA/ TiO_2 composites [35]. This

process results in an exchange of protons to form an unstable hemiaminals which were subsequently dehydrated to Schiff base [37]. The band at 1677 cm^{-1} $\delta(\text{H-O-H})$ can be ascribed to adsorbed water on the surface of the $\text{C}_{60}\text{-EDA/TiO}_2$ [6,7] which may be derived from unstable hemiaminal decomposition [35]. Therefore, the DOM, hemiaminal, Schiff base, formate, and carbonate are all the possible intermediate species during the process of formaldehyde adsorption and oxidation.

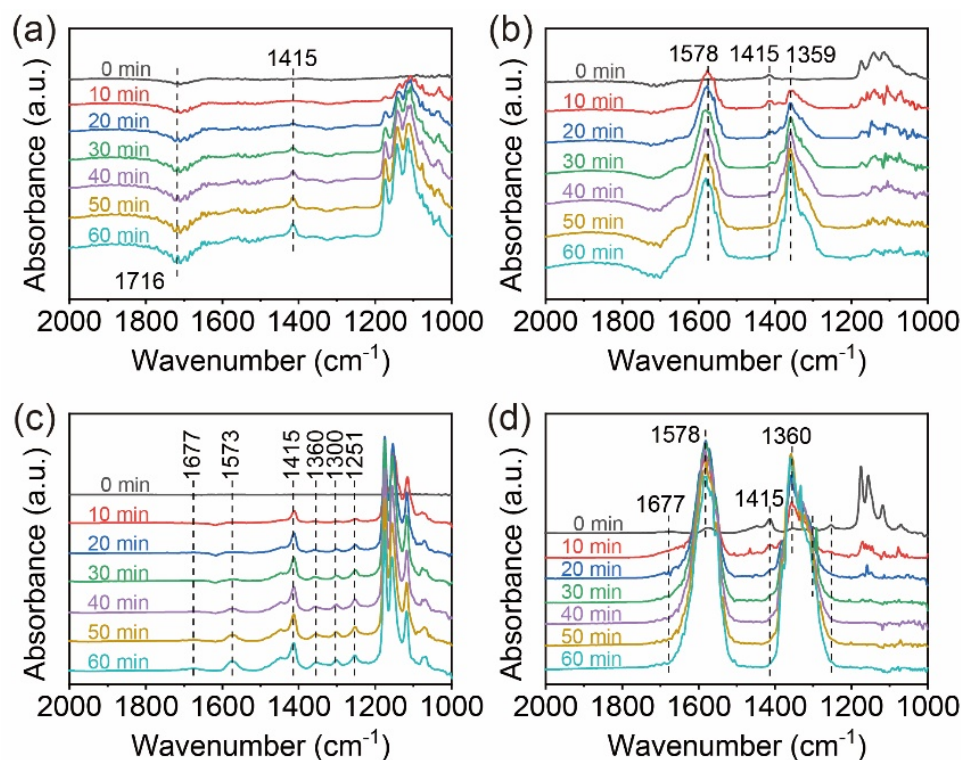


Figure 5. In situ DRIFT spectra of TiO_2 (a) before and (b) after illumination; $\text{C}_{60}\text{-EDA/TiO}_2$ (c) before and (d) after illumination.

Table 1. Infrared bands of surface species on TiO_2 or $\text{C}_{60}\text{-EDA/TiO}_2$, Derived from Figures 5 and S12.

Species	Assignment	Wavenumber (cm^{-1})	Refs.
DOM/Hemiaminal	$\nu(\text{CO})$	1114, 1174	[6,37]
	$\delta(\text{CH}_2)$	1415	
Formate/Carbonate	$\nu_s(\text{COO})$	1359	[6,7]
	$\nu_{as}(\text{COO})$	1578	
Hydroxy/Water	$\nu(\text{OH})$	3656, 3511, 3693	[6,55,56]
	$\delta(\text{OH})$	1716, 1677	
Hemiaminal/Imine	$\nu(\text{C-N})$	1251, 1300, 1360	[34,36,37]
	$\nu(\text{C=N})$	1573	

To analyze the contributions of $\text{C}_{60}\text{-EDA}$ and TiO_2 , the overall reaction of formaldehyde under dark or light on the surface of TiO_2 and $\text{C}_{60}\text{-EDA/TiO}_2$ is performed. The featured band of $\nu(\text{CO})$ was the product of the absorption of free HCHO molecules (Figure 6). In terms of the formaldehyde adsorption under dark (0~70 min), the peak intensity of $\nu(\text{OH})$ weakened gradually, $\nu(\text{CO})$ increased gradually, and $\nu_{as}(\text{COO})/\nu_s(\text{COO})$ were nearly not observed for pristine TiO_2 as the reaction took place (Figure 6a–c). It suggests that hydroxyl is gradually consumed and the HCHO that is adsorbed on the surface of the catalyst is converted into DOM [6,7]. It is worth noting that the peak intensity of the $\nu(\text{CO})$ of $\text{C}_{60}\text{-EDA/TiO}_2$ is significantly higher than that of the pristine TiO_2 (Figure 6b), but

the peak intensity of $\nu(\text{OH})$ does not decrease significantly in Figure 6a, indicating that the introduction of C_{60} -EDA reduced the consumption of hydroxyl. The increased production of $\nu(\text{CO})$ on the surface of the complex is due to the rapid chemisorption between the $-\text{NH}_2$ and HCHO . In addition, the peak intensity of $\nu(\text{CO})$ and $\nu(\text{C-N})$ increased rapidly for C_{60} -EDA/ TiO_2 during the reaction time of 0~30 min. Subsequently, the peak intensity of $\nu(\text{CO})$ decreased slowly, $\nu(\text{C-N})$ increased slowly, and $\nu(\text{C=N})$ increased rapidly at the reaction time of 30~70 min; the band at 3511 cm^{-1} (adsorbed water) gradually increased in Figure S12c. It turns out that formaldehyde is adsorbed on the surface of the C_{60} -EDA/ TiO_2 composite mainly through a reaction with the amino group. This process results in an exchange of protons to form an unstable hemiaminals which were subsequently dehydrated to form imines [37].

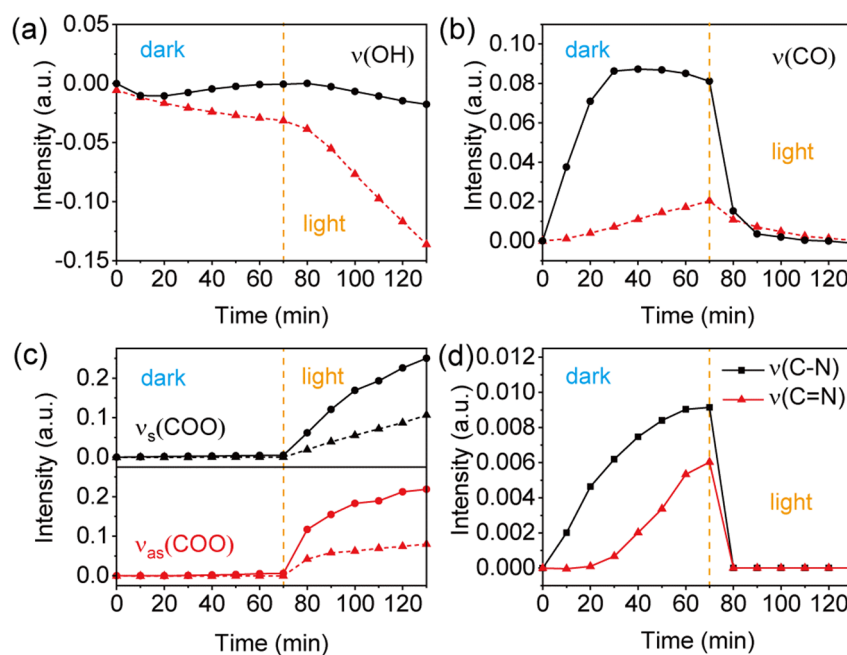
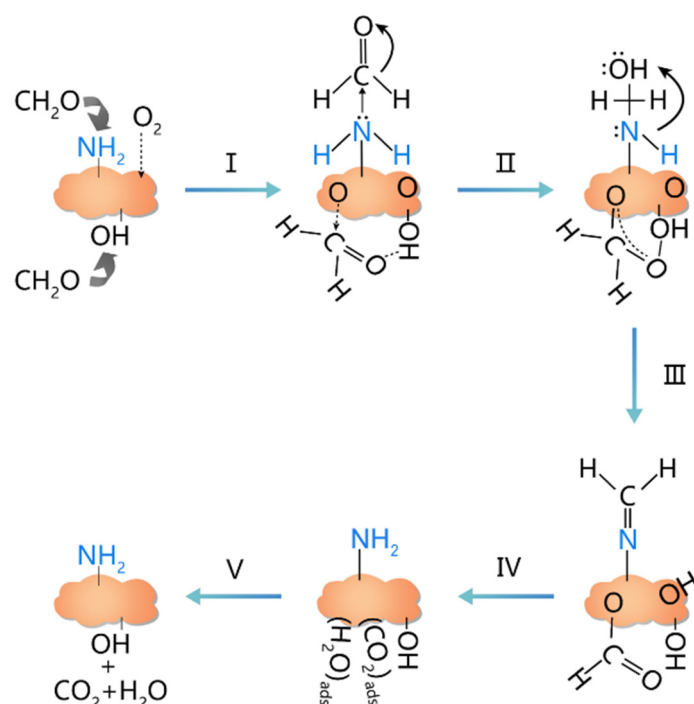


Figure 6. Peak intensities of surface species for formaldehyde adsorption and oxidation under dark (0~70 min) and light (70~130 min) as a function of the reaction time. (a) $-\text{OH}$ species; (b) C-O species; (c) COO species; (d) C-N/C=N species. The solid line is for C_{60} -EDA/ TiO_2 and the dashed line represents TiO_2 .

In terms of the reaction of formaldehyde oxidation of TiO_2 and C_{60} -EDA/ TiO_2 materials under light (70~130 min), the peak intensity of $\nu(\text{CO})$ and $\nu(\text{C-N/C=N})$ weakened rapidly (Figure 6b,d), and $\nu_{\text{as}}(\text{COO})/\nu_{\text{s}}(\text{COO})$ gradually increased (Figure 6c), indicating that the light promotes oxidative decomposition of DOM and hemiaminal/Schiff base to formate/carbonate species. It is worth noting that the $\nu(\text{C-N/C=N})$ basically disappeared completely after turning on the light source for 10 min (reaction time is 80 min) as shown in Figure 6d, while the peak intensity of $\nu(\text{CO})$ of C_{60} -EDA/ TiO_2 and TiO_2 has a similar trend (Figure 6b), indicating that both DOM and hemiaminal/Schiff base existed on the surface of the C_{60} -EDA/ TiO_2 composites, and hemiaminal/Schiff base is easier to oxidize to formate/carbonate species than DOM under light. Meanwhile, the peak intensity of $\nu_{\text{as}}(\text{COO})/\nu_{\text{s}}(\text{COO})$ on the surface of C_{60} -EDA/ TiO_2 composites is higher than that of pristine TiO_2 in Figure 6c, which further proves this conjecture. The results show that amino on the surface of C_{60} -EDA/ TiO_2 composites directly participates in the chemical adsorption and oxidation processes of HCHO .

Thus, a new insight into the reaction mechanism for the photocatalytic formaldehyde oxidation under simulated sunlight of C_{60} -EDA/ TiO_2 has been proposed in Scheme 1. HCHO is adsorbed on the surface of C_{60} -EDA/ TiO_2 composites by hydroxyl and amino group firstly (step I). Meanwhile, oxygen from air is adsorbed and splits into active oxygen

species on the surface of C_{60} -EDA/ TiO_2 composites. Then, the carbon (of carbonyl group) of HCHO is attacked by nucleophilic surface oxygen and active nitrogen atom on the surface of C_{60} -EDA/ TiO_2 to form DOM and hemiaminal (step II). Subsequently, unstable hemiaminals are dehydrated to form Schiff base (step III). DOM is oxidized to formate under simulated sunlight irradiation (step III). Subsequently, the formate acid and Schiff base is further oxidized into adsorbed CO_2 and H_2O by active oxygen radicals on the composites surface (step IV). Finally, the adsorbed CO_2 and water desorb from the composites surface, and hydroxyl and amino group active sites are regenerated again (step V). As we can see, the presence of C_{60} -EDA promotes the adsorption and oxidation of formaldehyde and improves the photocatalytic activity of the C_{60} -EDA/ TiO_2 composites (Figures S13–S17).



Scheme 1. Schematic diagram of the possible pathway for photocatalytic oxidation of formaldehyde over C_{60} -EDA/ TiO_2 under simulated sunlight.

4. Conclusions

A novel C_{60} -EDA/ TiO_2 nanocomposite was fabricated for the photocatalytic formaldehyde degradation efficiently. Comprehensive morphology studies along with surface and interface analyses have shed light on the interactions between C_{60} -EDA and TiO_2 nanoparticles, which play a vital role in the sunlight utilization and charge separation. The removal of formaldehyde should be divided into adsorption and catalytic oxidation processes. The exposed $-NH_2$ active groups in the C_{60} -EDA/ TiO_2 nanoparticles increased the adsorption ability of the formaldehyde molecule; some formaldehyde molecules combine with amino groups to form Schiff bases. Whereafter, the intermediate products Schiff base and DOM were oxidized to formate and carbonate by reactive oxygen on the surface, and then carbonate is decomposed into CO_2 and H_2O . The presence of C_{60} -EDA plays an important role in the rapid adsorption of free formaldehyde molecules and increases the photocatalytic activity. Briefly, this work realizes high-rate photocatalysis formaldehyde degradation at room temperature, paving a new way for obtaining high-efficiency indoor formaldehyde removal at ambient conditions.

Supplementary Materials: The following supporting information can be downloaded at: <https://www.mdpi.com/article/10.3390/nano12142366/s1>, Figure S1: Experimental apparatus for DRIFTS measurements; Figure S2: Schematic diagram of formaldehyde degradation device; Figure S3: SEM image of pristine TiO₂ nanoparticles; Figure S4. HRTEM image of C₆₀-EDA/TiO₂ composites; Figure S5: N1s XPS spectra of C₆₀-EDA and C₆₀-EDA/TiO₂ composite; Figure S6: Catalytic performance of pristine TiO₂ nanoparticles for photodegradation of HCHO under simulated sunlight irradiation; Figure S7: Catalytic performance of C₆₀-EDA/TiO₂ for photodegradation of HCHO under simulated sunlight irradiation. Formaldehyde concentration and CO₂ evolution amount with increasing photocatalytic time (Initial HCHO concentration at 100 ppm); Figure S8: Catalytic performance of the C₆₀-EDA/TiO₂ with different ratios of C₆₀-EDA for photodegradation of HCHO under simulated sunlight irradiation; Figure S9: SEM images of the C₆₀-EDA/TiO₂ sample before and after 12 cycles of the photocatalytic reactions; Figure S10: XRD spectra of C₆₀-EDA/TiO₂ before and after 12 cycles of the photocatalytic reactions; Figure S11: EPR spectra in (a) methanol dispersion system and (b) deionized water dispersion system; Figure S12: In situ DRIFT spectra of TiO₂ (a) before and (b) after illumination; C₆₀-EDA/TiO₂ (c) before and (d) after illumination; Table S1: Comparisons of the catalytic performances between C₆₀-EDA/TiO₂ and other reported formaldehyde catalysts; Figure S13. The molecular structures of the fullerene derivatives (a) C₆₀-EDA and (b) C₆₀-COOH; Figure S14. The XRD of TiO₂ and C₆₀-EDA/TiO₂ with comparison with standard PDF card of anatase titanium dioxide; Figure S15. Catalytic performance without photocatalyst and with C₆₀-EDA; Figure S16. Band gap energy diagram of (a) C₆₀-EDA and (b) C₆₀-COOH; Figure S17. XRD spectra of the C₆₀-EDA/TiO₂ with different ratios of C₆₀-EDA.

Author Contributions: Conceptualization, B.W. and C.W.; methodology, J.F.; validation, J.F., T.W. and B.W.; formal analysis, J.F. and T.W.; investigation, J.F.; resources, B.W. and C.W.; data curation, J.F.; writing—original draft preparation, J.F.; writing—review and editing, B.W.; supervision, C.W.; project administration, C.W.; funding acquisition, B.W. and C.W. All authors have read and agreed to the published version of the manuscript.

Funding: This research was funded by the National Natural Science Foundation of China, grant number 52072374, 51772300, and 51832008. B.W. particularly thanks the Youth Innovation Promotion Association of CAS (2018039).

Institutional Review Board Statement: Not applicable.

Informed Consent Statement: Not applicable.

Data Availability Statement: The data presented in this study are available on a reasonable request from the corresponding author.

Conflicts of Interest: The authors declare no conflict of interest.

References

1. Wang, Z.; Yu, H.; Xiao, Y.; Zhang, L.; Guo, L.; Zhang, L.; Dong, X. Free-standing composite films of multiple 2D nanosheets: Synergetic photothermocatalysis/photocatalysis for efficient removal of formaldehyde under ambient condition. *Chem. Eng. J.* **2020**, *394*, 125014–125024. [[CrossRef](#)]
2. Li, X.; Li, H.; Huang, Y.; Cao, J.; Huang, T.; Li, R.; Zhang, Q.; Lee, S.C.; Ho, W. Exploring the photocatalytic conversion mechanism of gaseous formaldehyde degradation on TiO_{2-x}-OV surface. *J. Hazard. Mater.* **2022**, *424*, 127217–127225. [[CrossRef](#)] [[PubMed](#)]
3. Xia, S.J.; Zhang, G.H.; Meng, Y.; Yang, C.; Ni, Z.M.; Hu, J. Kinetic and mechanistic analysis for the photodegradation of gaseous formaldehyde by core-shell CeO₂@LDHs. *Appl. Catal. B Environ.* **2020**, *278*, 119266–119278. [[CrossRef](#)]
4. Yuan, W.J.; Zhang, S.P.; Wu, Y.Y.; Huang, X.M.; Tian, F.H.; Liu, S.W.; Li, C.H. Enhancing the room-temperature catalytic degradation of formaldehyde through constructing surface lewis pairs on carbon-based catalyst. *Appl. Catal. B Environ.* **2020**, *272*, 118992–118999. [[CrossRef](#)]
5. Zhang, C.B.; He, H. A comparative study of TiO₂ supported noble metal catalysts for the oxidation of formaldehyde at room temperature. *Catal. Today* **2007**, *126*, 345–350. [[CrossRef](#)]
6. Zhu, X.; Jin, C.; Li, X.S.; Liu, J.L.; Sun, Z.G.; Shi, C.; Li, X.G.; Zhu, A.M. Photocatalytic Formaldehyde Oxidation over Plasmonic Au/TiO₂ under Visible Light: Moisture Indispensability and Light Enhancement. *ACS Catal.* **2017**, *7*, 6514–6524. [[CrossRef](#)]
7. Liu, Z.; Niu, J.; Long, W.; Cui, B.; Song, K.; Dong, F.; Xu, D. Highly Efficient MnO₂/AlOOH Composite Catalyst for Indoor Low-Concentration Formaldehyde Removal at Room Temperature. *Inorg. Chem.* **2020**, *59*, 7335–7343. [[CrossRef](#)]
8. Robert, B.; Nallathambi, G. Indoor formaldehyde removal by catalytic oxidation, adsorption and nanofibrous membranes: A review. *Environ. Chem. Lett.* **2021**, *19*, 2551–2579. [[CrossRef](#)]

9. Vipin, S.; Varun, G.; Paramvir, S.; Alok, G. Abatement of formaldehyde with photocatalytic and catalytic oxidation: A review. *Int. J. Chem. React. Eng.* **2020**, *19*, 1–29.
10. Adilah, S.; Salvador, E.; Thanita, A.; Hugo, D.L.; Siriluk, C. Photocatalytic Conversion of Organic Pollutants in Air: Quantum Yields Using a Silver/Nitrogen/TiO₂ Mesoporous Semiconductor under Visible Light. *Catalysts* **2021**, *11*, 529–555.
11. Yan, S.; Yu, J.; Zhu, B.; Qiao, K.; Cai, X.; Yuan, X.; Li, C. Photocatalytic Application of TiO₂-Loaded Viscose-Based Activated Carbon Fibers Composite Catalyst: Degradation of Low Concentration Formaldehyde and Simultaneous Anti-Microbe. *ECS J. Solid State Sc.* **2021**, *10*, 011002–011012. [[CrossRef](#)]
12. Pan, Y.; Liu, X.J.; Zhang, W.; Liu, Z.F.; Zeng, G.M.; Shao, B.B.; Liang, Q.H.; He, Q.Y.; Yuan, X.Z.; Huang, D.L.; et al. Advances in photocatalysis based on fullerene C₆₀ and its derivatives: Properties, mechanism, synthesis, and applications. *Appl. Catal. B Environ.* **2020**, *265*, 118579–118607. [[CrossRef](#)]
13. Lian, Z.; Xu, P.; Wang, W.; Zhang, D.; Xiao, S.; Li, X.; Li, G. C₆₀-decorated CdS/TiO₂ mesoporous architectures with enhanced photostability and photocatalytic activity for H₂ evolution. *ACS Appl. Mater. Inter.* **2015**, *7*, 4533–4540. [[CrossRef](#)] [[PubMed](#)]
14. Miyabe, H.; Kohtani, S. Photocatalytic single electron transfer reactions on TiO₂ semiconductor. *Sci. China Chem.* **2019**, *62*, 1439–1449. [[CrossRef](#)]
15. Wang, Z.; Xiong, F.; Zhang, Z.; Sun, G.; Xu, H.; Chai, P.; Huang, W. Surface Chemistry of Formaldehyde on Rutile TiO₂(011)-(2×1) Surface: Photocatalysis Versus Thermal-Catalysis. *J. Phys. Chem. C* **2017**, *121*, 25921–25929. [[CrossRef](#)]
16. Zhong, R.Y.; Zhang, Z.S.; Yi, H.Q.; Zeng, L.; Tang, C.; Huang, L.M.; Gu, M. Covalently bonded 2D/2D O-g-C₃N₄/TiO₂ heterojunction for enhanced visible-light photocatalytic hydrogen evolution. *Appl. Catal. B Environ.* **2018**, *237*, 1130–1138. [[CrossRef](#)]
17. Liu, L.; Liu, X.; Chai, Y.; Wu, B.; Wang, C. Surface modification of TiO₂ nanosheets with fullerene and zinc-phthalocyanine for enhanced photocatalytic reduction under solar-light irradiation. *Sci. China Mater.* **2020**, *63*, 2251–2260. [[CrossRef](#)]
18. Huo, P.; Shi, X.; Zhang, W.; Kumar, P.; Liu, B. An overview on the incorporation of graphene quantum dots on TiO₂ for enhanced performances. *J. Mater. Sci.* **2021**, *56*, 6031–6051. [[CrossRef](#)]
19. Chen, X.; Liu, L.; Yu, P.Y.; Mao, S.S. Increasing solar absorption for photocatalysis with black hydrogenated titanium dioxide nanocrystals. *Science* **2011**, *331*, 746–750. [[CrossRef](#)]
20. Nie, L.; Yu, J.; Li, X.; Cheng, B.; Liu, G.; Jaroniec, M. Enhanced performance of NaOH-modified Pt/TiO₂ toward room temperature selective oxidation of formaldehyde. *Environ. Sci. Technol.* **2013**, *47*, 2777–2783. [[CrossRef](#)]
21. Murdoch, M.; Waterhouse, G.I.; Nadeem, M.A.; Metson, J.B.; Keane, M.A.; Howe, R.F.; Llorca, J.; Idriss, H. The effect of gold loading and particle size on photocatalytic hydrogen production from ethanol over Au/TiO₂ nanoparticles. *Nat. Chem.* **2011**, *3*, 489–492. [[CrossRef](#)] [[PubMed](#)]
22. Quiroz Torres, J.; Royer, S.; Bellat, J.P.; Giraudon, J.M.; Lamonier, J.F. Formaldehyde: Catalytic oxidation as a promising soft way of elimination. *ChemSusChem* **2013**, *6*, 578–592. [[CrossRef](#)]
23. Yu, J.; Ma, T.; Liu, G.; Cheng, B. Enhanced photocatalytic activity of bimodal mesoporous titania powders by C₆₀ modification. *Dalton Trans.* **2011**, *40*, 6635–6644. [[CrossRef](#)] [[PubMed](#)]
24. Wang, S.; Liu, C.; Dai, K.; Cai, P.; Chen, H.; Yang, C.; Huang, Q. Fullerene C₇₀-TiO₂ hybrids with enhanced photocatalytic activity under visible light irradiation. *J. Mater. Chem. A* **2015**, *3*, 21090–21098. [[CrossRef](#)]
25. Virovska, D.; Paneva, D.; Manolova, N.; Rashkov, I.; Karashanova, D. Photocatalytic self-cleaning poly(l-lactide) materials based on a hybrid between nanosized zinc oxide and expanded graphite or fullerene. *Mater. Sci. Eng. C* **2016**, *60*, 184–194. [[CrossRef](#)]
26. Meng, Z.D.; Peng, M.M.; Zhu, L.; Oh, W.C.; Zhang, F.J. Fullerene modification CdS/TiO₂ to enhancement surface area and modification of photocatalytic activity under visible light. *Appl. Catal. B Environ.* **2012**, *113*, 141–149. [[CrossRef](#)]
27. Li, Q.; Xu, L.; Luo, K.-W.; Huang, W.-Q.; Wang, L.-L.; Li, X.-F.; Huang, G.-F.; Yu, Y.-B. Insights into enhanced visible-light photocatalytic activity of C₆₀ modified g-C₃N₄ hybrids: The role of nitrogen. *Phys. Chem. Chem. Phys.* **2016**, *18*, 33094–33102. [[CrossRef](#)]
28. Bai, X.J.; Wang, L.; Wang, Y.J.; Yao, W.Q.; Zhu, Y.F. Enhanced oxidation ability of g-C₃N₄ photocatalyst via C₆₀ modification. *Appl. Catal. B Environ.* **2014**, *152*, 262–270. [[CrossRef](#)]
29. Yao, S.; Yuan, X.; Jiang, L.; Xiong, T.; Zhang, J. Recent Progress on Fullerene-Based Materials: Synthesis, Properties, Modifications, and Photocatalytic Applications. *Materials* **2020**, *13*, 2924. [[CrossRef](#)]
30. Bai, W.; Krishna, V.; Wang, J.; Moudgil, B.; Koopman, B. Enhancement of nano titanium dioxide photocatalysis in transparent coatings by polyhydroxy fullerene. *Appl. Catal. B Environ.* **2012**, *125*, 128–135. [[CrossRef](#)]
31. Li, Q.; Hong, L.; Li, H.; Liu, C. Graphene oxide-fullerene C₆₀ (GO-C₆₀) hybrid for photodynamic and photothermal therapy triggered by near-infrared light. *Biosens. Bioelectron.* **2017**, *89*, 477–482. [[CrossRef](#)]
32. Meng, Z.D.; Zhu, L.; Ye, S.; Sun, Q.; Ullah, K.; Cho, K.Y.; Oh, W.C. Fullerene modification CdSe/TiO₂ and modification of photocatalytic activity under visible light. *Nanoscale Res. Lett.* **2013**, *8*, 189–198. [[CrossRef](#)]
33. Su, Y.; Chen, Z.-C.; Tian, H.-R.; Xu, Y.-Y.; Zhang, Q.; Xie, S.-Y.; Zheng, L.-S. Implications of Nitrogen Doping on Geometrical and Electronic Structure of the Fullerene Dimers. *Chin. J. Chem.* **2021**, *39*, 93–98. [[CrossRef](#)]
34. Na, C.J.; Yoo, M.J.; Tsang, D.C.W.; Kim, H.W.; Kim, K.H. High-performance materials for effective sorptive removal of formaldehyde in air. *J. Hazard. Mater.* **2019**, *366*, 452–465. [[CrossRef](#)]
35. Wu, K.; Kong, X.Y.; Xiao, K.; Wei, Y.; Zhu, C.C.; Zhou, R.; Si, M.T.; Wang, J.J.; Zhang, Y.Q.; Wen, L.P. Engineered Smart Gating Nanochannels for High Performance in Formaldehyde Detection and Removal. *Adv. Funct. Mater.* **2019**, *29*, 1807953. [[CrossRef](#)]

36. Wu, L.; Qin, Z.; Zhang, L.; Meng, T.; Yu, F.; Ma, J. CNT-enhanced amino-functionalized graphene aerogel adsorbent for highly efficient removal of formaldehyde. *New J. Chem.* **2017**, *41*, 2527–2533. [[CrossRef](#)]
37. Vikrant, K.; Cho, M.; Khan, A.; Kim, K.H.; Ahn, W.S.; Kwon, E.E. Adsorption properties of advanced functional materials against gaseous formaldehyde. *Environ. Res.* **2019**, *178*, 108672–108686. [[CrossRef](#)]
38. Liu, Q.; Yang, X.; Huang, Y.; Xu, S.; Su, X.; Pan, X.; Xu, J.; Wang, A.; Liang, C.; Wang, X.; et al. A Schiff base modified gold catalyst for green and efficient H₂ production from formic acid. *Energy Environ. Sci.* **2015**, *8*, 3204–3207. [[CrossRef](#)]
39. Carter, E.M.; Katz, L.E.; Speitel, G.E., Jr.; Ramirez, D. Gas-phase formaldehyde adsorption isotherm studies on activated carbon: Correlations of adsorption capacity to surface functional group density. *Environ. Sci. Technol.* **2011**, *45*, 6498–6503. [[CrossRef](#)]
40. Li, J.; Zhao, F.W.; Wang, T.S.; Nie, M.Z.; Li, J.J.; Wei, Z.X.; Jiang, L.; Wang, C.R. Ethylenediamine functionalized fullerene nanoparticles as independent electron transport layers for high-efficiency inverted polymer solar cells. *J. Mater. Chem. A* **2017**, *5*, 947–951. [[CrossRef](#)]
41. Lamparth, I.; Hirsch, A. Water-soluble Malonic Acid Derivatives of C₆₀ with a Defined Three-dimensional Structure. *J. Chem. Soc. Chem. Commun.* **1994**, *14*, 1727–1728. [[CrossRef](#)]
42. Zhang, H.; Zhou, P.; Ji, H.; Ma, W.; Chen, C.; Zhao, J. Enhancement of photocatalytic decarboxylation on TiO₂ by water-induced change in adsorption-mode. *Appl. Catal. B Environ.* **2018**, *224*, 376–382. [[CrossRef](#)]
43. Sheng, H.; Zhang, H.N.; Song, W.J.; Ji, H.W.; Ma, W.H.; Chen, C.C.; Zhao, J.C. Activation of Water in Titanium Dioxide Photocatalysis by Formation of Surface Hydrogen Bonds: An In Situ IR Spectroscopy Study. *Angew. Chem. Int. Ed.* **2015**, *54*, 5905–5909. [[CrossRef](#)]
44. Qi, K.Z.; Selvaraj, R.; Al Fahdi, T.; Al-Kindy, S.; Kim, Y.; Wang, G.C.; Tai, C.W.; Sillanpaa, M. Enhanced photocatalytic activity of anatase-TiO₂ nanoparticles by fullerene modification: A theoretical and experimental study. *Appl. Surf. Sci.* **2016**, *387*, 750–758. [[CrossRef](#)]
45. Xiong, M.; Tao, Y.; Zhao, Z.; Zhu, Q.; Jin, X.; Zhang, S.; Chen, M.; Li, G. Porous g-C₃N₄/TiO₂ foam photocatalytic filter for treating NO indoor gas. *Environ. Sci. Nano* **2021**, *8*, 1571–1579. [[CrossRef](#)]
46. Liu, S.-H.; Lin, W.-X. Heterostructured graphitic carbon nitride/titanium dioxide for enhanced photodegradation of low-concentration formaldehyde under visible light. *J. Photochem. Photobiol. A* **2019**, *378*, 66–73. [[CrossRef](#)]
47. Chechia, H.; Wei-Fan, T.; Wei-Han, W.; Kun-Yi Andrew, L.; Miao-Ting, L.; Keizo, N. Hydroxylation and sodium intercalation on g-C₃N₄ for photocatalytic removal of gaseous formaldehyde. *Carbon* **2021**, *175*, 467–477.
48. Yu, L.; Wang, L.; Sun, X.; Ye, D. Enhanced photocatalytic activity of rGO/TiO₂ for the decomposition of formaldehyde under visible light irradiation. *J. Environ. Sci.* **2018**, *73*, 138–146. [[CrossRef](#)]
49. Tang, D.; Zhang, G. Fabrication of AgFeO₂/g-C₃N₄ nanocatalyst with enhanced and stable photocatalytic performance. *Appl. Surf. Sci.* **2017**, *391*, 415–422. [[CrossRef](#)]
50. Song, S.; Lu, C.; Wu, X.; Jiang, S.; Sun, C.; Le, Z. Strong base g-C₃N₄ with perfect structure for photocatalytically eliminating formaldehyde under visible-light irradiation. *Appl. Catal. B Environ.* **2018**, *227*, 145–152. [[CrossRef](#)]
51. Liu, S.-H.; Lin, W.-X. A simple method to prepare g-C₃N₄-TiO₂/waste zeolites as visible-light-responsive photocatalytic coatings for degradation of indoor formaldehyde. *J. Hazard. Mater.* **2019**, *368*, 468–476. [[CrossRef](#)]
52. Liu, J.; Xiong, C.; Jiang, S.; Wu, X.; Song, S. Efficient evolution of reactive oxygen species over the coordinated π -delocalization g-C₃N₄ with favorable charge transfer for sustainable pollutant elimination. *Appl. Catal. B Environ.* **2019**, *249*, 282–291. [[CrossRef](#)]
53. Li, Y.; Wu, X.; Li, J.; Wang, K.; Zhang, G. Z-scheme g-C₃N₄@CsxWO₃ heterostructure as smart window coating for UV isolating, Vis penetrating, NIR shielding and full spectrum photocatalytic decomposing VOCs. *Appl. Catal. B Environ.* **2018**, *229*, 218–226. [[CrossRef](#)]
54. Li, X.; Qian, X.; An, X.; Huang, J. Preparation of a novel composite comprising biochar skeleton and “chrysanthemum” g-C₃N₄ for enhanced visible light photocatalytic degradation of formaldehyde. *Appl. Surf. Sci.* **2019**, *487*, 1262–1270. [[CrossRef](#)]
55. Lan, Z.; Yu, Y.; Yao, J.; Cao, Y. The band structure and photocatalytic mechanism of MoS₂-modified C₃N₄ photocatalysts with improved visible photocatalytic activity. *Mater. Res. Bull.* **2018**, *102*, 433–439. [[CrossRef](#)]
56. Huang, Q.; Wang, Q.; Tao, T.; Zhao, Y.; Wang, P.; Ding, Z.; Chen, M. Controlled synthesis of Bi₂O₃/TiO₂ catalysts with mixed alcohols for the photocatalytic oxidation of HCHO. *Environ. Technol.* **2019**, *40*, 1937–1947. [[CrossRef](#)]
57. Han, X.; Han, Z.; Zhao, J.; Zhao, X. Photocatalytic degradation of formaldehyde by PAN nonwoven supported Fe(III) catalysts under visible light irradiation. *New J. Chem.* **2017**, *41*, 9380–9387. [[CrossRef](#)]
58. Wang, Y.; Jiang, C.; Le, Y.; Cheng, B.; Yu, J. Hierarchical honeycomb-like Pt/NiFe-LDH/rGO nanocomposite with excellent formaldehyde decomposition activity. *Chem. Eng. J.* **2019**, *365*, 378–388. [[CrossRef](#)]
59. Qin, G.; Wu, X.; Zhang, H. Rational design of TiO₂-V₂O₅-C nanostructure grafted by N-doped graphene with enhanced photocatalysis and lithium ion store performances. *Rsc Adv.* **2014**, *4*, 52438–52450. [[CrossRef](#)]
60. Dou, H.L.; Long, D.; Rao, X.; Zhang, Y.P.; Qin, Y.M.; Pan, F.; Wu, K. Photocatalytic Degradation Kinetics of Gaseous Formaldehyde Flow Using TiO₂ Nanowires. *ACS Sustain. Chem. Eng.* **2019**, *7*, 4456–4465. [[CrossRef](#)]
61. Zhang, J.; Hu, Y.; Zheng, H.; Zhang, P. Hierarchical Z-scheme 1D/2D architecture with TiO₂ nanowires decorated by MnO₂ nanosheets for efficient adsorption and full spectrum photocatalytic degradation of organic pollutants. *Catal. Sci. Technol.* **2020**, *10*, 3603–3612. [[CrossRef](#)]
62. Fontmorin, J.M.; Burgos Castillo, R.C.; Tang, W.Z.; Sillanpaa, M. Stability of 5,5-dimethyl-1-pyrroline-N-oxide as a spin-trap for quantification of hydroxyl radicals in processes based on Fenton reaction. *Water Res.* **2016**, *99*, 24–32. [[CrossRef](#)]

63. Hu, Y.D.; Xie, X.F.; Wang, X.; Wang, Y.; Zeng, Y.; Pui, D.Y.H.; Sun, J. Visible-Light Upconversion Carbon Quantum Dots Decorated TiO₂ for the Photodegradation of Flowing Gaseous Acetaldehyde. *Appl. Surf. Sci.* **2018**, *440*, 266–274. [[CrossRef](#)]
64. Nomura, A.; Jones, C.W. Enhanced Formaldehyde-Vapor Adsorption Capacity of Polymeric Amine-Incorporated Aminosilicas. *Chem. Eur. J.* **2014**, *20*, 6381–6390. [[CrossRef](#)]